

Finite element modelling and static shape control of a functionally graded piezoelectric beam

I. ESHRAGHI

*School of Engineering Science, College of Engineering, University of Tehran,
P.O. Box 11155-4563, Tehran, Iran, e-mail: ieshraghi@ut.ac.ir*

A FINITE ELEMENT MODEL IS DEVELOPED for discretization and analysis of the functionally graded piezoelectric material (FGPM) beam based on the Timoshenko beam theory and assuming linear constitutive relation for the corresponding piezoelectric material behavior. Results obtained using the developed finite element code are compared with the available experimental and numerical results for smart structures with and without graded properties. Static shape control of the beam is conducted using the Buildup Voltage Distribution (BVD) algorithm by implementing this method in the finite element routine. Numerical simulations have been performed to study the performance of the shape control algorithm by optimizing the distribution of the applied voltages. Furthermore, the effect of the number of iterations on the result accuracy as well as the variation of the control voltage distribution with the number of discretized regions and the volume fractions of the constituent material is studied. A fast numerical convergence with good accuracy is observed for the shape control of FGPM beams using the developed method. The proposed technique is a good candidate for the modeling, analysis, and control of smart structures with graded properties.

Key words: functionally graded piezoelectric beams, finite element method, shape control, Buildup Voltage Distribution algorithm.



Copyright © 2023 The Author.

Published by IPPT PAN. This is an open access article under the Creative Commons Attribution License CC BY 4.0 (<https://creativecommons.org/licenses/by/4.0/>).

Notation

b	beam width,
$[B_{rb}], [B_{rs}], [B_{tb}], [B_{ts}]$	strain–displacement matrices,
$[B_p^i], [B_p^o]$	potential–electric field matrices,
$[C_b], [C_s]$	elasticity coefficients matrices,
$\{d_r\}, \{d_t\}$	generalized rotational and translational displacement variables,
$\{d_r^e\}, \{d_t^e\}$	generalized nodal rotational and translational displacement vectors,
dV	voltage added to (or subtracted from) current voltages of regions in each iteration in BVD algorithm,
D	electrical displacement vector,
$[e_b], [e_s]$	piezoelectric coefficient matrices,
$\{E_i\}, \{E_o\}$	electric field vectors,
E_P	total potential energy,
$[F_{tp}], [F_{rp}]$	global electro-elastic matrices,

$[F_{pt}^e], [F_{pr}^e], [F_{rp}^e], [F_{tp}^e]$	elemental electro-elastic coupling matrices,
h	beam thickness,
I_r, I_t	identity matrices,
$[K_{rr}], [K_{rt}], [K_{tr}], [K_{tt}]$	global stiffness matrices,
$[K_{rr}^e], [K_{rt}^e], [K_{tr}^e], [K_{tt}^e]$	elemental stiffness matrices,
$[K_D^e]$	elemental dielectric stiffness matrix,
L_{shape}	objective function of the BVD algorithm,
n_i	the shape function of natural coordinates associated with the node i ,
N_n	total number of nodes in BVD algorithm,
N_p	total number of regions in BVD algorithm,
$[N_r], [N_t]$	shape function matrices,
P	an effective material property of the beam,
P_U, P_V	material properties at the top and bottom surfaces of the beam,
$\{R\}$	global nodal mechanical force vector,
$\{R^e\}$	elemental load vector,
$[S]$	Influence Coefficient (IC) matrix in BVD algorithm,
SR	Selection Rate in BVD algorithm,
U, W	displacements along x and z axes,
u_0, w_0	generalized displacements of mid-line points along x and z axes,
V_U, V_L	volume fractions of FGPM constituent materials,
w_c^*	normalized calculated displacements of nodes at the current iteration in BVD algorithm,
w_d^*	normalized desired displacements of nodes in BVD algorithm,
$\{X_t\}, \{X_r\}$	global nodal generalized displacement vectors,
$\{\epsilon_b\}, \{\epsilon_s\}$	in-plane and transverse shear strain vectors,
$\{\epsilon_{bt}\}, \{\epsilon_{br}\}, \{\epsilon_{st}\}, \{\epsilon_{sr}\}$	generalized strain vectors,
$\epsilon_x, \epsilon_{xz}$	normal and transverse shear strains,
$[\eta_i], [\eta_o]$	dielectric permittivity coefficient matrices,
γ	parameter for selection of regions in BVD algorithm,
λ	volume fraction index of FGPM,
φ	electric potential function,
φ_0	generalized electric potential function of top surface,
$\{\varphi_0^p\}$	initial voltage distribution in BVD algorithm,
$\{\Phi\}$	global nodal electric potential vector,
ψ	generalized rotation of the normal to the mid-line,
$\{\sigma_b\}, \{\sigma_s\}$	in-plane and transverse shear stress vectors.

1. Introduction

PIEZOELECTRIC MATERIALS HAVE BEEN WIDELY USED as actuators and sensors for the design of smart structures and electromechanical systems [1]. Piezoelectric actuators and sensors are often made by bonding piezoelectric patches to achieve better performance and are often called layered piezoelectric materials. One issue of the layered piezoelectric patches is the creep of the bonding at elevated temperatures and existence of interfacial stress concentrations which result in microcrack initiation and propagation across the interface and as a result early failure of the structure [2]. Thus a class of piezoelectric ma-

materials, called functionally graded piezoelectric materials (FGPMs), has been introduced to resolve the issues of layered piezoelectric materials [3]. FGPMs have no distinct interfaces and their material properties vary continuously in one (or more) direction(s) [4]. The mechanical behavior analysis of FGPMs has been of great interest for researchers. SHARMA *et al.* [5] used the general differential quadrature method to assess the fundamental frequencies of exponentially FGPM beams. SHI and CHEN [6] derived analytical solutions for bending of cantilever FGPM beams subjected to different loadings. YANG and XIANG [7] used differential quadrature method to analyze the thermo-electro-mechanical behavior of monomorph, bimorph, and multimorph FGPM beams. KOMEILI *et al.* [8] used a combined finite element-Fourier series method for static analysis of functionally graded piezoelectric beams under various loading types and considering various beam theories. The first objective of this paper is to develop a finite element model for static bending analysis of FGPM beams considering shear effects. This model is then used for the purpose of the static shape control of the beam.

Smart structures with embedded or integrated piezoelectric sensors and actuators are often used for the vibration and shape control of structures. Shape control involves activating the structure in order to achieve a certain desired shape. Though shape control of smart structures is important, vibration control of smart structures made of FGPMs has been of more interest to the researchers [9–12]. Previous works have been focused on the shape control of structures using integrated or embedded piezoelectric actuators. KOCONIS *et al.* [13] were among the first to investigate the effect of input voltages for piezoelectric actuators on the shape control of smart structures. LIEW *et al.* [14, 15] used genetic algorithms and computational intelligence for shape control of functionally graded smart plates containing patches of piezoelectric sensors and actuators. They obtained the optimum voltage distribution for the open loop control as well as displacement gain values for the closed loop feedback control when patches located on one side of the plate were used as sensors. YU *et al.* [16] used laminated piezoelectric actuators for the shape control of a cantilever beam structure with a low control voltage. Assumptions of Timoshenko's beam theory and a linear constitutive law for describing piezoelectric material behavior were used in their work and laminated piezoelectric actuators were used for the purpose of shape control. Genetic algorithm was used to derive voltages of actuators. They concluded that over increasing the number of piezoelectric layers, suppression of the beam deformation improves. S. DA MOTA SILVA *et al.* [17] obtained numerical results for the shape control of composite structures with piezoelectric patches using the genetic algorithm and validated their results with the experimental data. Maximum error of fifteen percent was reported between their simulation and experimental results for obtaining the desired

shape. A more comprehensive review on the static and dynamic shape control of structures by piezoelectric actuation has been presented in the review work by IRSCHIK [18].

The second objective of this paper is the shape control of a functionally graded piezoelectric beam based on the linear piezoelectric theory. The Buildup Voltage Distribution (BVD) algorithm [19] has been used to determine the input voltage distribution across the beam surfaces. The method is implemented in the afore mentioned finite element model. Effects of the variation of volume fraction index and the number of regions on the applied voltage are examined. It is shown that the developed technique and its corresponding finite element code produce accurate results for the shape control of smart FGPM structures.

2. Functionally graded piezoelectric beam

Figure 1 shows a functionally graded piezoelectric beam of length L and height h in which x and z denote the longitudinal and through thickness directions of the beam, respectively. The material composition varies smoothly through the thickness of the beam structure. Here, it is assumed that the material composition varies continuously based on a power law distribution through the beam thickness; therefore, an effective material property (except for the Poisson ratio) can be defined as follows [20]:

$$(2.1) \quad P(z) = P_U V_U + P_L V_L,$$

where $P(z)$ is the effective material property of the beam, P_U and P_V are the material properties at the top and bottom of the beam, respectively, and V_U and V_L are the corresponding volume fractions of the materials defined by:

$$(2.2) \quad V_U = \left(\frac{z}{h} + \frac{1}{2} \right)^\lambda, \quad V_L = 1 - \left(\frac{z}{h} + \frac{1}{2} \right)^\lambda,$$

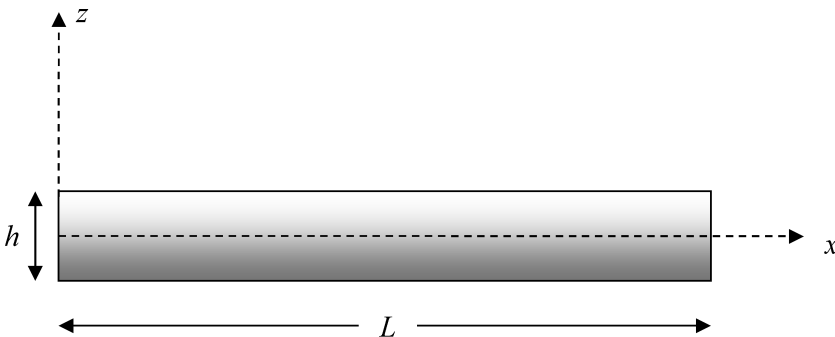


FIG. 1. Schematic diagram of a functionally graded piezoelectric beam.

where λ represents the volume fraction index of a functionally graded material. It should be noted that rule of mixtures used here to derive the effective material properties of FGPM may not yield accurate results as discussed in [20]. Other models such as the Mori–Tanaka micromechanics model [21] may be used to derive effective material properties, as it has no effect on the derivation of FE formulation and the shape control algorithm developed here. The use of rule of mixtures here is only because of its wide-spread use and the implementation simplicity.

According to the Timoshenko beam theory, the displacement field is given by [7]:

$$(2.3) \quad U(x, z) = u_0(x) + z\psi(x),$$

$$(2.4) \quad W(x, z) = w_0(x),$$

where U and W are the displacements of any point in the beam along the x and z axes, respectively; u_0 and w_0 are the generalized displacements of the point (x) on the mid-line ($z = 0$) in the respective directions, and ψ is the generalized rotation of the normal to the point x on the mid-line ($z = 0$). The generalized displacement variables can be separated into translational $\{d_t\}$ and rotational $\{d_r\}$ variables as follow [23]:

$$(2.5) \quad \{d_t\} = [u_0 \ w_0], \quad \{d_r\} = [\psi].$$

The strain field at any point of the beam is described by the in-plane strain component $\{\epsilon_b\}$ and the transverse shear strain component $\{\epsilon_s\}$ as follows:

$$(2.6) \quad \{\epsilon_b\} = [\epsilon_x], \quad \{\epsilon_s\} = [\epsilon_{xz}],$$

where ϵ_x is the normal strain along the x direction and ϵ_{xz} is the transverse shear strain. Assuming a linear strain–displacement relation, the in-plane strain vector $\{\epsilon_b\}$ and the transverse shear strain vector $\{\epsilon_s\}$ can be derived from Eq. (2.5) as follow:

$$(2.7) \quad \{\epsilon_b\} = \{\epsilon_{bt}\} + z\{\epsilon_{br}\}, \quad \{\epsilon_s\} = \{\epsilon_{st}\} + \{\epsilon_{sr}\},$$

where the generalized strain vectors $\{\epsilon_{bt}\}$, $\{\epsilon_{br}\}$, $\{\epsilon_{st}\}$, and $\{\epsilon_{sr}\}$ are given by:

$$(2.8) \quad \{\epsilon_{bt}\} = \left[\frac{\partial u_0}{\partial x} \right], \quad \{\epsilon_{br}\} = \left[\frac{\partial \psi}{\partial x} \right], \quad \{\epsilon_{st}\} = \left[\frac{\partial w_0}{\partial x} \right], \quad \{\epsilon_{sr}\} = [\psi].$$

For a piezoelectric material under the application of small elastic strains a linear constitutive relation can be assumed as follows [24]:

$$(2.9) \quad \sigma_{ij} = C_{ijkl}\epsilon_{kl} - e_{lij}E_l,$$

$$(2.10) \quad D_i = e_{ikl}\epsilon_{kl} - \eta_{il}E_l,$$

where σ_{ij} and ϵ_{kl} are the stress and strain tensors, respectively, D_i represents the electrical displacement vector, $E_l = -\varphi_{,l}$ is the electric field vector, and φ is the electric potential. C_{ijkl} denotes the fourth order elasticity tensor, e_{ikl} is the piezoelectric constant matrix, and η_{il} is the dielectric permittivity coefficient matrix. Using equations (2.7), (2.9), and (2.10), the set of linear constitutive relations for the piezoelectric material can be rewritten as follows:

$$(2.11) \quad \{\sigma_b\} = [C_b]\{\epsilon_b\} - [e_b]\{E_o\},$$

$$(2.12) \quad \{\sigma_s\} = [C_s]\{\epsilon_s\} - [e_s]\{E_i\},$$

$$(2.13) \quad \{D_o\} = [e_b]^T\{\epsilon_b\} + [\eta_o]\{E_o\},$$

$$(2.14) \quad \{D_i\} = [e_b]^T\{\epsilon_b\} + [\eta_o]\{E_o\}.$$

The elasticity matrices $[C_b]$ and $[C_s]$, the piezoelectric coefficient matrices $[e_b]$ and $[e_s]$, the dielectric permittivity coefficient matrix $[\eta]$ of piezoelectric materials used in this study are defined in the appendix.

It is assumed that the variation of the electric potential function φ across the thickness is linear; as a result, the electric potential function can be expressed as follows [23]:

$$(2.15) \quad \varphi(x, z) = \varphi_0(x) \left(\frac{z}{h} + \frac{1}{2} \right),$$

where φ_0 is the generalized electric potential function at any arbitrary point on the top surface of the beam.

3. Finite element formulation

The total potential energy of the FGPM beam is given by [23]:

$$(3.1) \quad E_P = \frac{1}{2} \left[\int_{\vartheta} (\{\epsilon_b\}^T \{\sigma_b\} + \{\epsilon_s\}^T \{\sigma_s\}) d\vartheta \right. \\ \left. - \int_{\vartheta} (\{E_o\}^T \{D_o\} + \{E_i\}^T \{D_i\}) d\vartheta \right] - \int_S \{d\}^T \{f_s\} dS - \{d\}^T \{f_c\},$$

where $\{f_s\}$ and $\{f_c\}$ are the externally applied surface traction vector acting over a surface area S and the external concentrated force, respectively, and ϑ represents the volume of the domain under consideration. Considering isoparametric line elements with three nodes for FE discretization of the beam and using Eq. (2.5), the general displacement vectors of the i^{th} ($i = 1, 2, 3$) node of the element can be expressed as follow:

$$(3.2) \quad \{d_{ti}\} = [u_{0i} \ w_{0i}]^T, \quad \{d_{ri}\} = [\psi_i].$$

Consequently, the generalized displacement vectors at any arbitrary point within the element can be written by:

$$(3.3) \quad \{d_t\} = [N_t]\{d_t^e\}, \quad \{d_r\} = [N_r]\{d_r^e\}.$$

The nodal generalized translational displacement vector $\{d_t^e\}$, the nodal generalized rotational displacement vector $\{d_r^e\}$ and the shape function matrices $[N_t]$ and $[N_r]$ are given by:

$$(3.4) \quad \{d_t^e\} = [\{d_{t1}\}^T \{d_{t2}\}^T \{d_{t3}\}^T]^T, \quad \{d_r^e\} = [\{d_{r1}\} \{d_{r2}\} \{d_{r3}\}]^T,$$

$$(3.5) \quad [N_t] = [N_{t1} \ N_{t2} \ N_{t3}], \quad [N_r] = [N_{r1} \ N_{r2} \ N_{r3}],$$

$$(3.6) \quad N_{ti} = n_i I_t, \quad N_{ri} = n_i I_r,$$

where, I_t and I_r are the identity matrices and n_i is the shape function of natural coordinates associated with the i^{th} node. Considering Eqs. (2.7), (2.8), and (3.3), the strain vectors at any point of the element can be expressed as follow:

$$(3.7) \quad \{\epsilon_b\} = [B_{tb}]\{d_t^e\} + z[B_{rb}]\{d_r^e\},$$

$$(3.8) \quad \{\epsilon_s\} = [B_{ts}]\{d_t^e\} + [B_{rs}]\{d_r^e\},$$

where the strain–displacement matrices $[B_{tb}]$, $[B_{rb}]$, $[B_{ts}]$, and $[B_{rs}]$ are given by:

$$(3.9) \quad [B_{tb}] = [B_{tb1} \ B_{tb2} \ B_{tb3}], \quad [B_{rb}] = [B_{rb1} \ B_{rb2} \ B_{rb3}],$$

$$(3.10) \quad [B_{ts}] = [B_{ts1} \ B_{ts2} \ B_{ts3}], \quad [B_{rs}] = [B_{rs1} \ B_{rs2} \ B_{rs3}],$$

where

$$(3.11) \quad [B_{tbi}] = \left[\frac{\partial n_i}{\partial x} \ 0 \right], \quad [B_{rbi}] = \frac{\partial n_i}{\partial x}, \quad [B_{tbi}] = \left[0 \ \frac{\partial n_i}{\partial x} \right], \quad [B_{rsi}] = n_i.$$

The generalized electric potential vector at any point within the element is given by

$$(3.12) \quad \varphi_0 = [N_\varphi]\{\varphi_0^e\},$$

where $\{\varphi_0^e\} = [\varphi_{01} \ \varphi_{02} \ \varphi_{03}]$ and $[N_\varphi] = [n_1 \ n_2 \ n_3]$. Using electric-potential relations in combination with Eqs. (2.15) and (3.12), the electric field vector is expressed in terms of the nodal generalized electric potential degrees of freedom $\{\varphi_0^e\}$ as follows:

$$(3.13) \quad \{E_i\} = [Z_p^i][B_p^i]\{\varphi_0^e\}, \quad \{E_o\} = [Z_p^o][B_p^o]\{\varphi_0^e\},$$

where $[Z_p^i] = -(\frac{z}{h} + \frac{1}{2})$, $[Z_p^o] = -(\frac{1}{h})$, $[B_p^i] = [B_{p1}^i \ B_{p2}^i \ B_{p3}^i]$ and $[B_p^o] = [B_{p1}^o \ B_{p2}^o \ B_{p3}^o]$. B_{pj}^i and B_{pj}^o are defined as follow:

$$(3.14) \quad [B_{pj}^i] = \left[\frac{\partial n_j}{\partial x} \right], \quad [B_{pj}^o] = [n_j].$$

Substituting Eqs. (2.11)–(2.14) into (3.1) and using (3.7), (3.8), and (3.13), the total potential energy (E_P^e) of a typical element of the FGPM beam is obtained as follows:

$$(3.15) \quad E_P^e = \frac{1}{2} [\{d_t^e\}^T [K_{tt}^e] \{d_t^e\} + \{d_t^e\}^T [K_{tr}^e] \{d_r^e\} + \{d_r^e\}^T [K_{rt}^e] \{d_t^e\} + \{d_r^e\}^T [K_{rr}^e] \{d_r^e\} - \{d_t^e\}^T [F_{tp}^e] \{\varphi_0^e\} - \{d_r^e\}^T [F_{rp}^e] \{\varphi_0^e\} - \{\varphi_0^e\}^T [F_{pt}^e] \{d_t^e\} - \{\varphi_0^e\}^T [F_{pr}^e] \{d_r^e\} - \{\varphi_0^e\}^T [K_D^e] \{\varphi_0^e\}] - \{d_t^e\}^T \{R^e\}.$$

The elemental stiffness matrices $[K_{tt}^e]$, $[K_{tr}^e]$, $[K_{rt}^e]$, and $[K_{rr}^e]$, the elemental electro-elastic coupling matrices $[F_{tp}^e]$, $[F_{rp}^e]$, $[F_{pt}^e]$ and $[F_{pr}^e]$, the elemental dielectric stiffness matrix $[K_D^e]$, and the elemental load vector $\{R^e\}$ are defined in the appendix. It is worth mentioning that decoupled formulations for the elemental bending and shear stiffness matrices are used here and as a result a selective integration scheme can be adopted to evaluate the corresponding element matrices. Upon applying the principle of minimum total potential energy, i.e., $\delta E_P^e = 0$, the following governing equilibrium equations for an element can be obtained:

$$(3.16) \quad [K_{tt}^e] \{d_t^e\} + [K_{tr}^e] \{d_r^e\} = [F_{tp}^e] \{\varphi_0^e\} + \{R^e\},$$

$$(3.17) \quad [K_{rt}^e] \{d_t^e\} + [K_{rr}^e] \{d_r^e\} = [F_{rp}^e] \{\varphi_0^e\}.$$

For the purpose of shape control, electric potential (voltage) is applied at the top and bottom of the beam. Therefore, $\delta \{\varphi_0^e\} = 0$, which leads to the derivation of the above governing equations for each discretized element. Upon assembling the equations and considering the element nodal continuity, the global equations of equilibrium are written as follow:

$$(3.18) \quad [K_{tt}] \{X_t\} + [K_{tr}] \{X_r\} = [F_{tp}] \{\Phi\} + \{R\},$$

$$(3.19) \quad [K_{rt}] \{X_t\} + [K_{rr}] \{X_r\} = [F_{rp}] \{\Phi\},$$

where, $[K_{tt}]$, $[K_{tr}]$, $[K_{rt}]$, and $[K_{rr}]$ are the global stiffness matrices, $[F_{tp}]$ and $[F_{rp}]$ are the global electro-elastic matrices, $\{X_t\}$ and $\{X_r\}$ are the global nodal generalized displacement vectors, $\{R\}$ is the global nodal mechanical force vector, and $\{\Phi\}$ is the global nodal electric potential vector. Over imposing the displacement boundary conditions, the global rotational degrees of freedom are

condensed to obtain the global equilibrium equations in terms of the global translational degrees of freedom only, i.e.:

$$(3.20) \quad [K]\{X_t\} = [F_{tp}^*]\{\Phi\} + \{R\}$$

in which, $[K] = [K_{tt}] - [K_{tr}][K_{rr}]^{-1}[K_{rt}]$ and $[F_{tp}^*] = [F_{tp}] - [K_{tr}][K_{rr}]^{-1}[F_{rp}]$. Equation (3.20) represents the electro-elastic finite element model of the functionally graded piezoelectric beam considered in this work.

4. Validation of the developed finite element code

A MATLAB code has been developed for implementation of the FE formulation of the FGPM beam described in the previous section. The accuracy of the proposed finite element model and its corresponding developed FE code for functionally graded piezoelectric beams is considered first. In what follows, three examples have been solved in order to evaluate the accuracy of the developed FE code by comparing its results with the available theoretical and numerical results of the literature.

4.1. Cantilever KYNAR piezoelectric beam

As shown in Fig. 2, a cantilever beam consisting of two layers of KYNAR piezoelectric films is considered. The relevant material properties are given in [25]. The effect of the applied voltage on the tip deflection have been studied and compared with the results obtained by KOCONIS *et al.* [13]. Eight elements were used for modeling of the beam. Figure 3 shows the comparison between the predicted results by the developed FE simulation with the available experimental data given in [13]. It is observed that results obtained by the developed FE code considering eight elements are in excellent agreement with those of the experimental data reported by KOCONIS *et al.* [13].

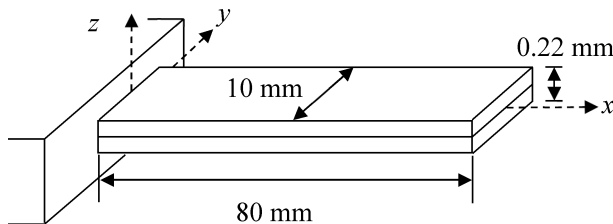


FIG. 2. Schematic of a KYNAR cantilever piezoelectric beam.

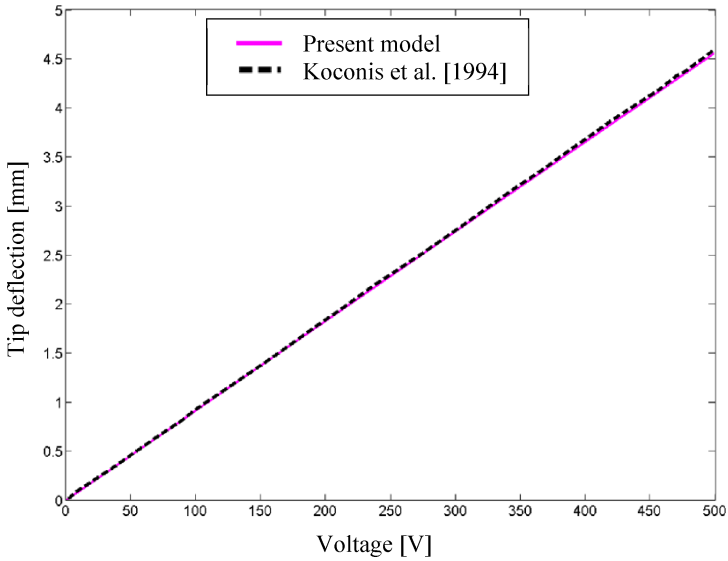


FIG. 3. Tip deflection of (piezoelectric KYNAR) cantilever beam as a function of input voltage.

4.2. Static deformation of a functionally graded beam

For the second verification case, static deformation of a functionally graded beam with simply supported ends is considered here. FG material of the beam is composed of Aluminum (Al; $E_m = 70 \text{ GPa}$, $\nu_m = 0.3$) and Zirconia (ZrO_2 ; $E_c = 200 \text{ GPa}$, $\nu_c = 0.3$) and its properties vary according to Eq. (2.1) through the thickness. The bottom surface of the beam is considered to be pure Zirconia and the top one is considered to be pure Aluminum. The beam width and thickness are assumed to be constant with values $b = 0.1 \text{ m}$ and $h = 0.1 \text{ m}$, respectively.

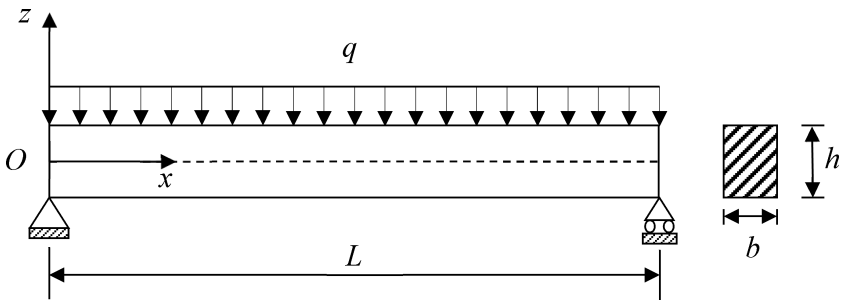


FIG. 4. A functionally graded simply-supported beam under uniformly distributed load.

Two different values for the beam length are considered in the FE simulation, i.e., 0.4 m and 1.6 m with 8 and 16 beam elements used for beam discretization, respectively. Distributed loading with the intensity of q is applied at the top surface as shown in Fig. 4. The lateral deflection of the middle section of the beam is normalized by dividing it to the maximum lateral deflection of a homogeneous beam made of Aluminum which is obtained from the analytical relation $w_{stat} = 5qL^4/384c_{11}^A I$.

Results obtained from the presented FE model are compared with the results presented by ŞİMŞEK [26], and are summarized in Table 1. Good agreement is observed between the results of the current FE formulation and the Ritz method results presented by ŞİMŞEK [26].

TABLE 1. Maximum non-dimensional lateral tip deflection of the beam for various values of volume fraction index.

FGM index	Normalized Lateral Deflection			
	$L/h = 16$		$L/h = 4$	
	Present model	ŞİMŞEK [26]	Present model	ŞİMŞEK [26]
$\lambda = 0.0$ (Aluminium)	1.14286	1.13002	1.00893	1.00812
$\lambda = 0.2$	0.85842	0.85842	0.75614	0.75595
$\lambda = 0.5$	0.72268	0.71482	0.63995	0.63953
$\lambda = 1.0$	0.63602	0.62936	0.56657	0.56615
$\lambda = 2.0$	0.56739	0.56165	0.50754	0.50718
$\lambda = 5.0$	0.49680	0.49176	0.44423	0.44391
100% Ceramic	0.40007	0.39550	0.35319	0.35284

4.3. Static deformation of a cantilever bimorph beam

As the last set of verification cases, the free end displacement of a cantilever bimorph piezoelectric beam with $L/h = 6$ and subjected to a uniform distributed load of $q = 10 \text{ kN/m}^2$ and an applied voltage of $V = 100 \text{ V}$ is investigated in Table 2. Analytic results from YANG and XIANG [7] are presented in this table for comparison. Ten elements are used for beam discretization. The bimorph actuator has two layers of piezoelectric material with opposite polarizations with the following material properties:

$$C_{11} = 60.6 \text{ GPa}, \quad C_{55} = 23 \text{ GPa},$$

$$d_{31} = -274 \times 10^{-12} \text{ C/N}, \quad d_{15} = 741 \times 10^{-12} \text{ C/N}.$$

Excellent agreement is observed between the results of current formulation and the analytical results of [7].

TABLE 2. Free end deflection of a bimorph cantilever beam subjected to electro-mechanical loads.

Load	Free end deflection [m]	
	Present model	Yang and Xiang [7]
$q = 10 \text{ kN/m}^2$	3.286×10^{-4}	3.286×10^{-4}
$V=100 \text{ V}$	14.796×10^{-7}	14.796×10^{-7}

5. Shape control algorithm

The Buildup Voltage Distribution (BVD) algorithm is employed here for the purpose of the shape control of the FGPM beam. The top surface of the beam structure is discretized into a number of regions and the bottom surface is assumed to be grounded. Each region is constructed of at least one element and each element must be fully covered by only one region. In each region, the magnitude of the voltage applied for the shape control is constant. The primary objective of shape control analysis is to find the magnitude of the applied voltage in each region in order to deform the beam to a predefined and desired shape. Generally, the desired shape of the structure is known prior to the analysis either through a specified mathematical function or by a prescribed displacement field to the beam nodes. The general process of the shape control using the BVD algorithm as proposed by CHEE *et al.* [19] is explained in this section through a step-by-step procedure.

The relation between the transverse nodal displacement $\{w_0\}$ vector $[N_n \times 1]$ and the voltage distribution $\{\varphi^p\}$ vector $[N_p \times 1]$ is given by:

$$(5.1) \quad \{w_0\} = [S]\{\varphi^p\} = \sum_{k=1}^{N_p} \{S_k\}\varphi_k^p = \{S_1\}\varphi_1^p + \{S_2\}\varphi_2^p + \cdots + \{S_{N_p}\}\varphi_{N_p}^p,$$

where N_n is the total number of nodes, N_p is the total number of regions, $[S]$ is the influence coefficient (IC) matrix, and $\{S_k\}$ is the IC column vector. The linearity between the displacements and voltages, as a result of the linear constitutive equation employed here, allows expressing $\{w_0\}$ as a linear combination of $\{\varphi^p\}$. Each $\{S_k\}$ vector can be obtained as the displacement vector $\{w_0\}$ assuming that all of the voltages are zero except $\varphi_k^p = 1$.

Suppose that the corresponding transverse nodal displacement of the desired shape of the beam is denoted by $\{w_d\}$. An initial voltage distribution vector $\{\varphi^p\}_0$ is applied to the regions and the corresponding nodal displacements vector $\{w_{(j=0)}\}$ are calculated using Eq. (5.1). Three types of initial voltage distribution may be applied. (1) All region voltages are set to zero initially. (2) A random set of voltages is applied. (3) A user defined set of voltages is applied initially.

An incremental voltage value denoted by dV is also selected. The incremental voltage dV should be set to the same order of magnitude to the initial voltage distribution.

The “ L_{shape} ” variable, which is the sum of all the squared differences of the transverse displacements between the desired and the actual (calculated) shape at all nodes, is defined as the objective function for the BVD algorithm. This variable is calculated during the j^{th} iteration ($j = 1, 2, \dots$) of the algorithm as:

$$(5.2) \quad 0 < L_{shape} = \sum_{i=1}^{N_n} (w_{di}^* - w_{(j)i}^*)^2 < 4N_n,$$

where w_i is the transverse displacement at the i^{th} node and superscript $*$ denotes quantities normalized by their corresponding maximum values. During each iteration, a selected number of the total active regions are chosen and their voltages are increased by a certain amount of dV . Selection of these regions is based on the γ value given by:

$$(5.3) \quad 0 < \gamma_{(j)}^{(m^\pm)} = \frac{1}{4} \sum_{i=1}^{N_n} c_{ij} (w_{di}^* - w_{(j)i}^{*(m^\pm)})^2 < N_n,$$

where

$$c_{ij} = \left[\frac{(w_{di}^* - w_{(j-1)i}^*)}{\text{Max}_{\forall i} \{|(w_{di}^* - w_{(j-1)i}^*)|\}} \right]^2.$$

$\{w_{(j)}^{(m^\pm)}\}$ is the vector of nodal transverse displacements calculated in the j^{th} iteration by adding (or subtracting) dV to the $|m|^{\text{th}}$ row of the voltage distribution vector of the previous iteration. Starting the iteration from $j = 1$, the following quantities are calculated:

$$\begin{aligned} \gamma_{(j)}^{(m^+)} \dots & \quad \text{for } m^+ = 1, 2, \dots, N_p, \\ \gamma_{(j)}^{(m^-)} \dots & \quad \text{for } m^- = -1, -2, \dots, -N_p, \end{aligned}$$

where

$$\gamma_{(j)}^{(m^\pm)} = f(\{w_{(j)}^{m^\pm}\}) = f(\{w(\{\varphi_{(m^\pm)}^p\}_{(j)})\})$$

and

$$\{\varphi_{(m^\pm)}^p\}_{(j)} = \{\varphi^p\}_{(j-1)} \pm dV \cdot \{\varphi^p\}_m^I,$$

where $\{\varphi^p\}_m^I$ is a zero vector except for the $|m^\pm|^{\text{th}}$ row in which it is equal 1. A selection rate value, SR , in the range of 0 to 0.5 is assumed. The selection rate, SR , is a parameter that determines the number of regions, N_s , to be selected

among $2N_p$ cases that were tested in this step, i.e., $N_s = \text{Integer}(SR \times 2N_p)$. The selected number of regions with the lowest $\gamma_{(j)}$ values will have dV permanently added (or subtracted) on the existing voltage vector of the previous iteration.

The procedure of computing $\gamma_{(j)}$ values, selection of regions, and modifying the voltages based on the new configuration of voltages is repeated for a fixed number of iterations or until the solution is converged to the desired shape (i.e., L_{shape} becomes less than a predefined value tol). The step-by-step implementation of the algorithm is as follows:

1. A desired shape for the beam is given w_d .
2. Divide the beam surface into N_p regions.
3. Calculate the influence coefficient (IC) matrix $[S]$ using the developed FE code by applying an input voltage of unit magnitude to each region and obtaining the corresponding lateral displacements of the beam nodes.
4. Select values for the selection rate ($0 < SR < 0.5$), the initial voltage vector φ_0 and the incremental voltage (dV).
5. From Eq. (5.1) calculate the corresponding initial deformation of the beam $w_{(0)}$.
6. Set $j = 1$.
7. Store current voltage distribution in the vector φ .
8. From Eq. (5.2) calculate L_{shape} using normalized values of $w_{(0)}$ and w_d .
9. While $L_{shape} > tol$ do the following:
 - (a) Calculate c_{ij} using the normalized values of w_d and $\{w_{(j-1)}\}$.
 - (b) For $i = 1 : N_p$ do:
 - i. $m^+ = i$.
 - ii. Add dV to the i^{th} row of $\{\varphi\}$ and store it in $\{\varphi^+\}$, i.e., $\{\varphi^+\} = \{\varphi\} + dV_i$.
 - iii. Calculate $\{w_{(j)}^{m^+}\} = [C]\{\varphi^+\}$.
 - iv. Calculate $\gamma_{(j)}^{(m^+)}$ using Eq. (5.3) and the normalized values of w_d and $\{w_{(j)}^{m^+}\}$.
 - (c) For $i = 1 : N_p$ do:
 - i. $m^- = -i$.
 - ii. Subtract dV from the i^{th} row of φ and store it in φ^- , i.e., $\{\varphi^-\} = \{\varphi\} - dV_i$.
 - iii. Calculate $\{w_{(j)}^{m^-}\} = [C]\{\varphi^-\}$.
 - iv. Calculate $\gamma_{(j)}^{(m^-)}$ using Eq. (5.3) and the normalized values of w_d and $\{w_{(j)}^{m^-}\}$.

- (d) From the $2N_p$ cases of $\gamma_{(j)}$ calculated in steps b and c select $N_s = \text{Integer}(SR \times 2N_p)$ cases with the lowest $\gamma_{(j)}$ values and permanently add (or subtract) dV to the corresponding region and update the $\{\varphi\}$ vector.
- (e) Calculate $\{w_{(j)}\} = [C]\{\varphi\}$.
- (f) Set $j = j + 1$.
- (g) Calculate L_{shape} using Eq. (5.2).

10. End.

It must be noted that if a region is selected twice, which represents a positive and a negative electric field, the one with the greater γ value is discarded. Moreover, if the iteration becomes trapped into two alternating voltage distributions, then dV will be halved. Selection of dV and SR essentially affects on the number of iterations required to achieve converged solution. In order to reach the desired shape in a smaller number of iterations and with more accuracy it is possible to apply the algorithm in a specified number of iterations with an arbitrary selected SR , dV , and starting voltages values. The results of this pre-run, may be used as the starting applied voltage in the main execution of the algorithm.

5.1. Numerical results of shape control

This section illustrates results obtained for the shape control of a cantilever FGPM beam. PZT-4 and PZT-5H are selected as the material models of the FGPM material. It is assumed that the top surface of the beam is 100% PZT-4 and the bottom surface is 100% PZT-5H. The material properties for PZT-4 and PZT-5H are given in Table 3 which are taken from [7]. The beam has a length of 200 mm and a uniform rectangular cross section with a width of 20 mm and a thickness of 5 mm. The beam is clamped at the left end as shown in Fig. 5. In this figure the numbers indicate the equipotential regions used for shape control implementation. Such equipotential surfaces have been discussed and used earlier for modeling equipotential surfaces in [27, 28]. The BVD algorithm is employed to control the shape of the beam for the following two cases. In the first case, the beam is subjected to a mechanical load and the shape control algorithm must return the beam to its undeformed configuration. In the second case, a desired mathematical shape is given and the control algorithm must deform the structure in a way that it closely matches the predefined desired shape. The top surface of the beam is divided into ten regions and the beam is divided evenly into 40 elements along the x direction. Each region consists of four elements and the magnitude of the applied voltage is constant through each region.

Firstly, it is assumed that the beam is subjected to a distributed downward load of 10 N/m^2 . The objective is to find the distribution of the applied voltage

TABLE 3. Material properties of PZT-4 and PZT-5H [7].

Property	PZT-4	PZT-5H
C_{11} [GPa]	139	126
C_{55} [GPa]	25.6	23.0
e_{31} [C/m ²]	-5.2	-6.5
e_{15} [C/m ²]	12.7	17.0

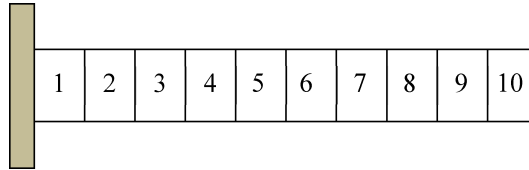


FIG. 5. Schematic top view of cantilevered functionally graded piezoelectric beam with discretized regions.

across the ten regions such that the deflection of the structure under the influence of the load is suppressed to zero. The deformation of the structure under the applied load for $\lambda = 1.0$ and the normalized shape of the beam when the shape control algorithm is employed are shown in Fig. 6 for different iteration numbers.

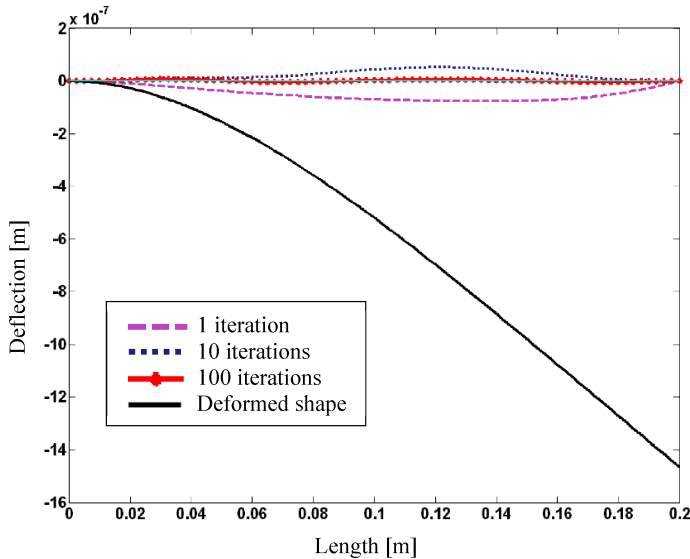


FIG. 6. Desired shape and transverse deflection of the centerline of the beam using BVD shape control algorithm with different number of iterations.

The initial voltage distribution is taken to be 10 volts on all regions and the SR value is considered to be 0.3. A magnitude of 5 volts is used for the incremental voltage increase, dV .

As shown in Fig. 6, over increasing the number of iterations for calculating the required voltage, the normalized transverse displacement of the beam tends to zero. Values of the mean square errors of the obtained beam shapes with the desired shape after various iterations are summarized in Table 4. It can be seen that the mean square error rapidly decreases by increasing the number of iterations.

TABLE 4. Mean square errors of the obtained beam shapes with the desired shape for different iteration numbers.

Number of iterations	Mean square error ($\times 10^{-17}$) [m ²]
1	895.1620
5	496.0748
10	391.4066
50	8.6242
100	3.8692

The effect of volume fraction index on the required voltages for the shape control of the FGPM beam is summarized in Table 5. From this table, it is observed that the magnitudes of the required voltages first decrease by increasing the volume fraction index up to the value of $\lambda = 1.0$, and then increase over further increase of the index value. This is because the induced flexural deflection of the beam under the applied electrical load is related to the variation of the piezoelectric coefficient, e_{31} , across the beam thickness. If there were no variation of this coefficient across the beam thickness, there would be no transverse deflection through the beam length (this corresponds to a purely PZT-4 or PZT-5H beam).

TABLE 5. Variation of the voltage distribution with the volume fraction index for a cantilever FGPM beam.

Volume fraction index	Region voltages [V]									
	V_1	V_2	V_3	V_4	V_5	V_6	V_7	V_8	V_9	V_{10}
$\lambda = 0.2$	592.4	230.3	271.1	375.1	111.4	74.3	46.4	-22.3	104.0	37.1
$\lambda = 0.5$	338.8	131.7	155.1	214.5	63.7	42.5	26.5	-12.7	59.5	21.24
$\lambda = 1.0$	268.5	104.4	122.9	170.0	50.5	33.7	21.0	-10.1	47.1	16.8
$\lambda = 2.0$	264.0	102.7	120.9	167.2	49.7	33.1	20.7	-9.9	46.4	16.6
$\lambda = 5.0$	363.6	141.3	166.4	230.2	68.4	45.6	28.5	-13.7	63.8	22.8
$\lambda = 10$	566.7	220.3	259.4	358.9	106.6	71.1	44.4	-21.3	99.5	35.5

Increasing the value of λ from 0.2 to 1.0 makes the beam more inhomogeneous and as a result the magnitude of the required voltage decreases. Further increase of the volume fraction index results in more homogeneity of the beam by PZT-4 material and thus less variation of e_{31} through the thickness which results in the increase of the required voltage for the transverse deflection of the beam.

As the second case, the effect of the number of regions on the shape control of the FGPM beam is investigated. The desired shape of the beam is shown in Fig. 7 and is predefined by the mathematical relation

$$w_d = \frac{\cos\left(\frac{2\pi x}{L}\right) - 1}{10^7}.$$

No mechanical load is applied to the beam in this case. The upper surface of the beam is divided into 2, 4, 8, and 10 regions and a value of 0.3 is assigned to SR . Also, a magnitude of 10 volts is considered for the incremental voltage increase, dV . The initial voltage distribution of regions for each case is given in Table 6.

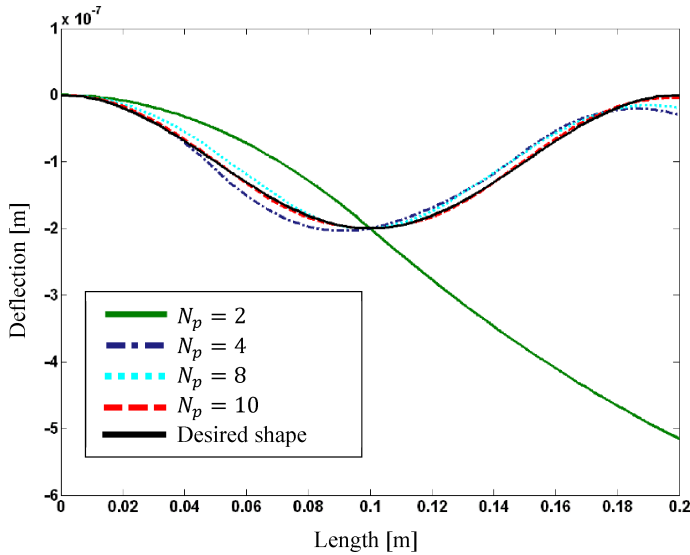


FIG. 7. Desired shape and transverse deflection of the centerline of the beam using BVD shape control algorithm with different number of regions.

Results obtained for the shape control of the beam with different number of regions are shown in Fig. 7 for the case of $\lambda = 1.0$ and an overall number of 100 iterations. Magnitudes of required voltages of regions are summarized in Table 7. It is obvious that over increasing the number of regions from two to four, the accuracy of the algorithm improves, remarkably. However, such improvement

TABLE 6. Initial voltage distribution for different number of regions.

Number of regions	Initial voltage distribution [V]									
	V_1	V_2	V_3	V_4	V_5	V_6	V_7	V_8	V_9	V_{10}
2	-50	50	-	-	-	-	-	-	-	-
4	-50	-40	40	50	-	-	-	-	-	-
8	-50	-40	0	60	60	0	-40	-50	-	-
10	-50	-40	0	60	50	50	60	0	-40	-50

TABLE 7. Variation of voltage distribution for different number of regions of the FGPM beam.

Number of regions	Region voltages [V]									
	V_1	V_2	V_3	V_4	V_5	V_6	V_7	V_8	V_9	V_{10}
2	-70.6	30.6	-	-	-	-	-	-	-	-
4	-157.7	-189.5	89.9	-174.3	-	-	-	-	-	-
8	-117.9	-114.1	30.9	213.7	172.9	22.6	-111.6	-161.5	-	-
10	-147.6	-119.2	-20.6	147.9	135.2	137.5	143.2	-25.6	-125.2	-155.5

is relatively small for further increase of the regions to more than four. Since there are two inflection points in the desired shape of the structure, i.e., three changes in the beam curvature, at least three regions must be considered in order to apply the external voltage and achieve the desired shape. Furthermore, symmetry of the required voltages is obvious for the case of $N_p = 10$. Values of the mean square errors of the obtained beam shapes with the desired shape for different number of regions after 100 iterations are summarized in Table 8. It can be observed that the mean square error decreases as the number of regions are raised. Best results are obtained when 10 regions are employed for the purpose of shape control.

Note that as may be observed from the presented results, large actuation voltages have been applied to control the shape of FGPM beams. It is to be noted that at large applied potentials, the behavior of the piezoelectric materials is nonlinear (piezoelectric coupling coefficients are functions of applied

TABLE 8. Mean square errors of the obtained beam shapes with the desired shape for different number of regions.

Number of regions (N_p)	Mean square error ($\times 10^{-17}$) [m^2]
2	1065.3460
4	16.8170
8	9.3421
10	0.5386

voltages) [29, 30]. However, the main focus of the current study is on the demonstration of the integrated FE+BVD formulation for shape control of FGPM beams. These structures have practical use in smart micro-electro-mechanical devices in which the values of applied loads and corresponding displacements are small and thus the assumptions of linearity of the behavior of the material used here are justified.

6. Conclusions

In this work, finite element modeling of FGPM beams and their corresponding shape control using the Buildup Voltage Distribution algorithm were considered. The developed finite element code was validated with the available analytical and/or experimental data and the its corresponding accuracy was verified. The developed finite element model is capable of considering variation of both the mechanical and electrical properties and can be used to model homogeneous as well as inhomogeneous beams made of isotropic and/or anisotropic material properties. Effect of shear deformation was also considered and consequently shearing and bending stiffness matrices were formed and calculated separately using the selective integration technique. In order to control the FGPM beam shape to achieve a desired shape, the BVD shape control algorithm was employed in the developed FE code. The FE code with the BVD algorithm implemented in it was used to calculate the required applied voltage distribution for FGPM beams which yields a predefined desired shape for the corresponding beams.

Numerical simulations were carried out for the shape control of monomorph FGPM beams. The effect of volume fraction index and the number of regions were studied on the required voltage and it was demonstrated that volume fraction index has non-intermediate effect on the voltage distribution which leads to lower control voltage for intermediate values of volume fraction indices. It was also shown that for a predefined desired shape, the minimum required number of regions to be considered to achieve an acceptable and accurate shape equals to the number of the curvature changes in the prescribed desired shape. Increasing the number of regions beyond this value showed negligible effect on attaining the prescribed desired shape of the structure and only improved numerical accuracy. The effect of number of iterations on the precision of the algorithm was also evaluated. Furthermore, using the functionally graded piezoelectric materials the possibility of self-shape-controlling of the structure by applying appropriate voltage distribution and without bonding or embedding piezoelectric patches was demonstrated in this work.

Theoretically it is possible to achieve any desired shape (compatible with the boundary conditions and physical constraints of the beam) with increasing

the number of elements and corresponding active zones of the structure. However, there are certain limitations from the practical point of view that prevents achieving such flexibility in real applications. These limitations include but not limited to challenges in applying the voltages, nonlinear behavior of piezoelectric materials, breaking the assumptions used here in approximating mechanical and electrical behavior of the structure.

The present work can be well extended to modeling and static or dynamic analysis of FGPM plates and shells and their corresponding shape control or vibration control.

Appendix. Elemental matrices

Vectors of stress, electrical displacement, and electric field and elasticity matrices, piezoelectric coefficient matrices, dielectric permittivity coefficient matrix of PZT materials are expressed as follows:

$$(A.1) \quad \begin{aligned} \{\sigma_b\} &= \sigma_x, & \{\sigma_s\} &= \sigma_{xz}, \\ \{D_i\} &= D_x, & \{D_o\} &= D_z, \\ \{E_i\} &= E_x, & \{E_o\} &= E_z, \\ [C_b] &= C_{11}, & [C_s] &= C_{55}, \\ [e_b] &= e_{31}, & [e_s] &= e_{15}, \\ [\eta_i] &= \eta_{11}, & [\eta_o] &= \eta_{33}. \end{aligned}$$

Elemental stiffness, electro-elastic coupling, and dielectric stiffness matrices, and the elemental load vector in Eq. (3.15) are given as:

$$(A.2) \quad [K_{tt}^e] = [K_{ttb}^e] + [K_{tts}^e], \quad [K_{tr}^e] = [K_{trb}^e] + [K_{trs}^e],$$

$$(A.3) \quad [K_{rr}^e] = [K_{rrb}^e] + [K_{rrs}^e], \quad [K_{rt}^e] = [K_{tr}^e]^T,$$

$$(A.4) \quad [K_{ttb}^e] = b_e \int_0^{l_e} [B_{tb}]^T [D_{tb}] [B_{tb}] dx, \quad [K_{tts}^e] = b_e \int_0^{l_e} [B_{ts}]^T [D_{ts}] [B_{ts}] dx$$

$$(A.5) \quad [K_{trb}^e] = b_e \int_0^{l_e} [B_{tb}]^T [D_{trb}] [B_{rb}] dx, \quad [K_{trs}^e] = b_e \int_0^{l_e} [B_{ts}]^T [D_{trs}] [B_{rs}] dx,$$

$$(A.6) \quad [K_{rrb}^e] = b_e \int_0^{l_e} [B_{rb}]^T [D_{rrb}] [B_{rb}] dx, \quad [K_{rrs}^e] = b_e \int_0^{l_e} [B_{rs}]^T [D_{rrs}] [B_{rs}] dx,$$

$$(A.7) \quad [F_{tp}^e] = [F_{tpb}^e] + [F_{tps}^e], \quad [F_{rp}^e] = [F_{rpb}^e] + [F_{rps}^e],$$

$$(A.8) \quad [F_{pt}^e] = [F_{tp}^e]^T, \quad [F_{pr}^e] = [F_{rp}^e]^T,$$

$$(A.9) \quad [F_{tpb}^e] = b_e \int_0^{l_e} [B_{tb}]^T [D_{tpb}] [B_p^o] dx, \quad [F_{tps}^e] = b_e \int_0^{l_e} [B_{ts}]^T [D_{tps}] [B_p^i] dx,$$

$$(A.10) \quad [F_{rpb}^e] = b_e \int_0^{l_e} [B_{rb}]^T [D_{rpb}] [B_p^o] dx, \quad [F_{rps}^e] = b_e \int_0^{l_e} [B_{rs}]^T [D_{rps}] [B_p^i] dx,$$

$$(A.11) \quad [K_D^e] = [K_{Di}^e] + [K_{Do}^e],$$

$$(A.12) \quad [K_{Di}^e] = b_e \int_0^{l_e} [B_p^i]^T [D_{Di}] [B_p^i] dx, \quad [K_{Do}^e] = b_e \int_0^{l_e} [B_p^o]^T [D_{Do}] [B_p^o] dx,$$

$$(A.13) \quad \{R^e\} = b_e \int_0^{l_e} [N_t]^T \{f_s\} dx + \{f_c\},$$

where l_e and b_e denote the length and the width of the element. The rigidity terms are:

$$(A.17) \quad [D_{tb}] = \int_{-h/2}^{h/2} [C_b] dz, \quad [D_{ts}] = \int_{-h/2}^{h/2} [C_s] dz,$$

$$(A.18) \quad [D_{trb}] = \int_{-h/2}^{h/2} z [C_b] dz, \quad [D_{trs}] = [D_{ts}],$$

$$(A.19) \quad [D_{rrb}] = \int_{-h/2}^{h/2} z^2 [C_b] dz, \quad [D_{rrs}] = [D_{ts}],$$

$$(A.20) \quad [D_{tpb}] = \int_{-h/2}^{h/2} [e_b] [Z_p^o] dz, \quad [D_{tps}] = \int_{-h/2}^{h/2} [e_s] [Z_p^i] dz,$$

$$(A.21) \quad [D_{rpb}] = \int_{-h/2}^{h/2} z [e_b] [Z_p^o] dz, \quad [D_{rps}] = [D_{tps}],$$

$$(A.22) \quad [D_{Do}] = \int_{-h/2}^{h/2} [Z_p^o]^T [\eta_o] [Z_p^o] dz, \quad [D_{Di}] = \int_{-h/2}^{h/2} [Z_p^i]^T [\eta_i] [Z_p^i] dz.$$

References

1. S.S. RAO, M. SUNAR, *Piezoelectricity and its use in disturbance sensing and control of flexible structures: a survey*, Applied Mechanics Reviews, **47**, 113–123, 1994.
2. Z. ZHONG, E.T. SHANG, *Three-dimensional exact analysis of a simply supported functionally gradient piezoelectric plate*, International Journal of Solids and Structures, **40**, 5335–5352, 2003.
3. C.C.M. WU, M. KAHN, W. MOY, *Piezoelectric ceramics with functional gradients: a new application in material design*, Journal of American Ceramics Society, **79**, 809–812, 1996.
4. W.F. SHELLEY II, S. WAN, K.J. BOWMAN, *Functionally graded piezoelectric ceramics*, Material Science Forum, 308–311, 515–520, 1999.
5. P. SHARMA, B. GUPTA, S. K. RATHORE, A. KHINCHI, M. GAUTAM, *Computational characteristics of an exponentially functionally graded piezoelectric beam*, International Journal on Interactive Design and Manufacturing, 1–7, 2022.
6. Z.F. SHI, Y. CHEN, *functionally graded piezoelectric cantilever beam under load*, Archive of Applied Mechanics, **74**, 237–247, 2004.
7. J. YANG, H.J. XIANG, *Thermo-electro-mechanical characteristics of functionally graded piezoelectric actuators*, Smart Materials and Structures, **16**, 784–797, 2007.
8. A. KOMEILI, A.H. AKBARZADEH, A. DOROUSHI, M.R. ESLAMI, *Static analysis of functionally graded piezoelectric beams under thermo-electro-mechanical loads*, Advances in Mechanical Engineering, **3**, 153731, 2011.
9. B.G. FITZPATRICK, *Shape matching with smart material structures using piezoceramic actuators*, Journal of Intelligent Material Systems and Structures, **8**, 876–882, 1997.
10. B.N. AGRAWAL, K.E. TREANOR, *Shape control of statically indeterminate laminated beams with piezoelectric actuators*, Smart Materials and Structures, **8**, 729–740, 1999.
11. M. KEKANA, *A static shape control model for piezo-elastic composite structures*, Composite Structures, **59**, 129–135, 2003.
12. M. KEKANA, P. TABAKOV, *Static control of composite plates using piezoelectric sensor and actuator techniques*, Smart Materials and Structures, **14**, 349–353, 2005.
13. D.B. KOCONIS, L.P. KOLLAR, *Shape control of composite plates and shells with embedded actuators. I. Voltages specified*, Journal of Composite Materials, **28**, 5, 415–458, 1994.
14. K.M. LIEW, X.Q. HE, R. TAPABRATA, *On the use of computational intelligence in the optimal shape control of functionally graded smart plates*, Computer Methods in Applied Mechanics and Engineering, **193**, 4475–4492, 2004.
15. K.M. LIEW, X.Q. HE, S.A. MEGUID, *Optimal shape control of functionally grade smart plates using genetic algorithms*, Computational Mechanics, **33**, 245–253, 2004.
16. Y. YU, X.N. ZHANG, S.L. XIE, *Optimal shape control of a beam using piezoelectric actuators with low control voltage*, Smart Material and Structures, **18**, 095006, 2009.
17. S. DA MOTA SILVA, R. RIBEIRO, J. DIAS RODRIGUES, M.A.P. VAZ, J.M. MONTEIRO, *The application of genetic algorithms for shape control with piezoelectric patches – an experimental comparison*, Smart Materials and Structures, **13**, 220–226, 2004.

18. H. IRSCHIK, *review on static and dynamic shape control of structures by piezoelectric actuation*, Engineering Structures, **24**, 5–11, 2002.
19. C. CHEE, L. TONG, G. STEVEN, *A buildup voltage distribution (BVD) algorithm for shape control of smart plate structures*, Computational Mechanics, **26**, 115–128, 2000.
20. S. KAPURIA, M. BHATTACHARYYA, A.N. KUMAR, *Bending and free vibration response of layered functionally graded beams: a theoretical model and its experimental validation*, Composite Structures, **82**, 3, 390–402, 2008.
21. T. MORI, K. TANAKA, *Average stress in matrix and average elastic energy of materials with misfitting inclusions*, Acta Metallurgica, **21**, 5, 571–574, 1973.
22. K.M. LIEW, X.Q. HE, T.Y. NG, S. SIVASHANKER, *Active control of FGM plates subjected to a temperature gradient: Modeling via finite element method based on FSDT*, International Journal of Numerical Methods in Engineering, **52**, 1253–1271, 2001.
23. M.C. RAY, H.M. SACHADE, *Finite element analysis of smart functionally graded plates*, International Journal of Solids and Structures, **43**, 5468–5484, 2006.
24. K.M. LIEW, X.Q. HE, T.Y. NG, S. KITIPORNCHAI, *Finite element piezothermoelasticity analysis and the active control of FGM plates with integrated piezoelectric sensors and actuators*, Computational Mechanics, **31**, 350–358, 2002.
25. M. SHAKERI, S.N. SADEGHI, M. JAVANBAKHT, H. HATAMIKIAN, *Dynamic analysis of functionally graded plate integrated with two piezoelectric layers, based on a three-dimensional elasticity solution*, Proceedings of the Institution of Mechanical Engineers, Part C: Journal of Mechanical Engineering Science, **223**, 1297–1309, 2009.
26. M. SIMSEK, *Static analysis of a functionally graded beam under a uniformly distributed load by Ritz method*, International Journal of Engineering and Applied Sciences, **1**, 1–11, 2009.
27. S. KAPURIA, M.Y. YASIN, *Active vibration control of piezoelectric laminated beams with electroded actuators and sensors using an efficient finite element involving an electric node*, Smart Materials and Structures, **19**, 4, 045019, 2010.
28. M.Y. YASIN, B. PRAKASH, A.H. KHAN, *Finite element model based on an efficient layerwise theory for dynamics and active vibration control of smart functionally graded beams*, Materials Research Express, **7**, 2, 025703, 2020.
29. Q.M. WANG, Q. ZHANG, X. BAOMIN, L. RUIBIN, L.E. CROSS, *Nonlinear piezoelectric behavior of ceramic bending mode actuators under strong electric fields*, Journal of Applied Physics, **86**, 6, 3352–3360, 1999.
30. M.Y. YASIN, B. PRAKASH, N. UR RAHMAN, M.N. ALAM, A.H. KHAN, *Design, fabrication, nonlinear analysis, and experimental validation for an active sandwich beam in strong electric field and thermal environment*, Journal of Sound and Vibration, 117828, 2023.

Received May 9, 2023; revised version July 11, 2023.

Published online September 13, 2023.